White Paper

Characteristics of the

xSPECT reconstruction method

A. Hans Vija, PhD
SPECT Research and Development
Siemens Healthineers, Molecular Imaging Business Line

siemens.com/healthineers

SIEMENS Healthineers

Motivation to change the reconstruction method and paradigm

In 2013, Siemens introduced xSPECT™, which represents a more complete integration of SPECT and CT data as compared to conventional SPECT/CT systems. In contrast to such systems, xSPECT not only amalgamates SPECT and CT data by adopting a point-of-view centered on the anatomical modality, but also adopts a strictly data-centered perspective, whereby the system's image formation characteristics are first measured, and this information is then applied during the reconstruction in image space. The guiding principles behind xSPECT are to take better advantage of the structural information imparted by the higher spatial resolution of the CT, and to build a quantitative reconstruction engine from the ground up. The underlying technology improves the multi-modal alignment in image space, enhances image quality and opens a pathway to further integrate system- and application-specific contextual information into the reconstructing of tomographic emission data. We hold the future of SPECT to entail full quantitation, as this will best support both diagnostic and theranostic applications.

Absolute quantitation is an essential feature of xSPECT. The injected activity becomes distributed throughout the patient or phantom prior to the time of acquisition, and may thus be regarded as a functional activity density with the preferred SI units of Bq/ml (note: 1 kBq/ml=Bq/mm^3). Any measurement is associated with a measurement error. We attempt to minimize this error whenever possible, with the first step being to constrain the error of the injection dose measurement, and next to cross-calibrate the imaging system with an absolute standard. Thus, we provide a 3% National Institute of Standards and Technology (NIST)-traceable calibration source for sensitivity calibrations of the system, serving also for cross-calibration of the dose calibrator. xSPECT thereby provides standardization limiting the variation in quantification of all Symbia Intevo™ and Symbia Intevo Bold™ SPECT/CT scanners. The other steps in the image reconstruction entail a careful design of the image formation, where the paradigm is shifted from correction of data prior to reconstruction to correction within image space. The reconstruction method is based on ordered subset conjugate gradient method (OSCG) and detailed in reference 1.

Noise is an important property of any reconstruction, and much work has been devoted to studying noise, e.g., behavior in aid of iterative reconstruction methods such as Maximum Likelihood Expectation Maximization (MLEM).[2-9] In references 2-4, the authors developed a theoretical model and a Monte Carlo simulation method to study statistical properties of MLEM. Additionally, comparisons of statistical properties and convergence rates between MLEM and Weighted Least Squares-Conjugated Gradient (WLS-CG) have been investigated.[2, 10, 11]

Resolution is another image property that is integral to the performance of an algorithm. For Filtered Back-Projection (FBP), it is sufficient to measure a modulation transfer function (MTF), which may be derived from simple point or line sources.[12, 13] However, it is known that the resolution of iteratively reconstructed images is spatially- and source-dependent,[14, 15] and the authors of reference 16 have shown that characterization of the resolution by traditional means is insufficient. In this regard, the resolution properties of our xSPECT method, which can incorporate extra modal information (EMI) into the reconstruction, is of key importance.

The proposed method considers many edges in reconstructed images of a complex, extended phantom, and is motivated by reference 17. The performance of xSPECT is compared to Flash 3D (OSEM3D),[18] which has been the standard in clinical practice.

Quantitative assessment is already important in oncology for internal dosimetry,[19, 20] where it can now be used for radionuclide treatment planning and monitoring, and may perhaps in the future find new applications in tumor grading and staging. Evaluation of quantitation accuracy of xSPECT is discussed in the second part of this paper.

In 2016, we expanded the quantitative xSPECT formalism traceable to NIST beyond ^{99m}Tc and LEHR to ^{99m}Tc and ^{123}I on the low penetration collimator for low energy (LPHR), and for ^{111}In and ^{177}Lu on our medium energy (ME) collimator. We also introduced quantitative SPECT using our xSPECT technology for all other isotopes and parallel hole collimators (Broad Quantification™), and a sophisticated cross-calibration scheme to support cross-calibration using multiple dose calibrators. xSPECT Quant™ uses the same approach as introduced for ^{99m}Tc xSPECT Quant in 2013, but adapted for the isotope and collimator combinations by using either a NIST-traceable ^{57}Co source or ^{75}Se source, and by using the respective measured PSF on the LPHR and ME collimators with factory-set energy window settings. We give the clinical user tools and flexibility to quantitatively acquire other isotope configurations, albeit not in all cases yet traceable to NIST. In principle, one can use the same methods to measure noise and resolution described here for the other isotopes, at the cost of prolonged handling of ^{177}Lu, ^{123}I or ^{111}In to fill the phantoms.

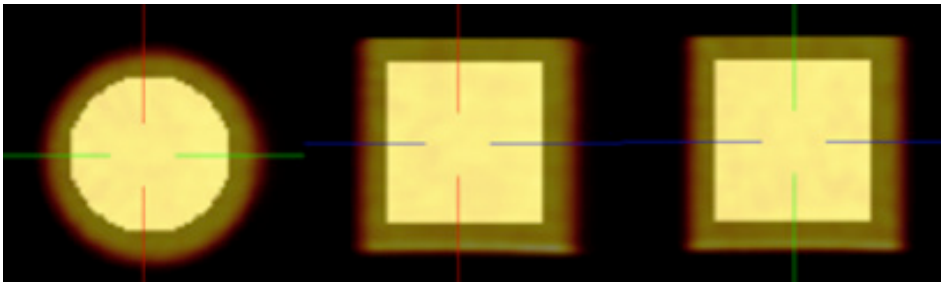

Figure 1: Volume of interest (VOI) inside uniform cylinder phantom for noise measurement. The light yellow cylinder inside the phantom is the selected VOI.

Noise and resolution characteristics

Methods and materials

The proposed measurement for noise and resolution is generic, and is based on edge-derived image resolution.[21, 22] Two different settings are used for the assessment: (1) a uniform cylinder phantom to measure noise in conjunction with a Hot-Cold-Rod (HCR) phantom to measure resolution; and (2) a Hot-Cold-Sphere (HCS) phantom to measure noise and resolution, simultaneously. The HCR and HCS phantom have the same vessel dimension as the uniform phantom but contain different inserts, per vendor specifications.

Setting 1: Uniform Cylinder+HCR

Ideally, it is preferable to measure noise and resolution within one phantom. However, the commercially available HCS[23] lacks a section sufficiently uniform and large to afford reliable noise measurement; consequently, we measure noise for the uniform cylinder phantom.

The ratio of standard deviation (SD) over the mean within a large 3D volume-of-interest (VOI) in a uniform phantom is used as the noise metric. We chose a large and long enough VOI (typically 8 cm radius and 16 cm length) centered within the phantom (so placed as to avoid edges), thus minimizing partial volume effects, as shown in Figure 1, where the exact dimensions of the VOI do not matter.

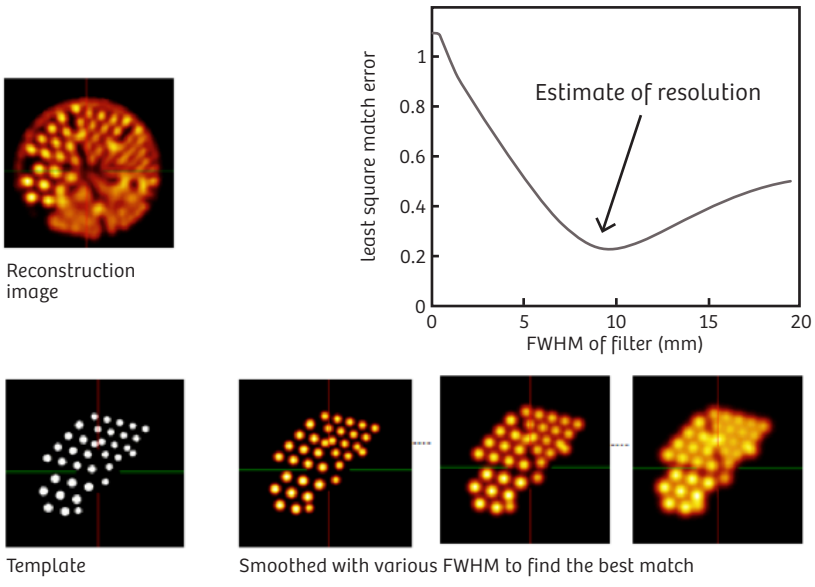

Figure 2: Illustration of resolution measurement using matched filter for HCR. Given a real reconstructed image, the template is smoothed with Gaussian filters of various FWHM, and the difference square between the real image and filtered template is calculated. The FWHM, which gives the smallest difference, is recognized as the resolution.

To assess resolution, we used a matched filter approach, as follows. For a reconstructed image in hot rod regions, we employed a high-resolution template derived from the CT with a series of Gaussian filters of various widths defined by their respective full width at half maximum (FWHM). Then, each of these smoothed templates was compared to the same slices in the nuclear reconstructions. The resolution is defined as the FWHM which yields the least squared difference as measured with the objective function where I is the real image, T is the template, Fh is the Gaussian filter with FWHM (h) and O is the set of slices chosen in hot rod regions of a HCR phantom as shown in Figure 2.

$$E_h = \frac{\sqrt{\sum_{x \in O}\left(I(x) - T * F_h(x)\right)^2}}{\sqrt{\sum_{x \in O}\left(I(x)\right)^2}}$$

The image intensity values of the template are assigned based on the activity concentration in the rods. Five slices in the hot regions are used, and for each slice a 2-D Gaussian smoothing in matched filter assessment is carried out. Only the three largest sections are considered, because the remaining three sections are not separable by traditional SPECT reconstruction methods, and their inclusion would bring non-correctible bias.

Unlike the FWHM of a point or a line source in a cold or warm background, the present approach is better suited to compare images from various modalities and reconstruction methods. One could even further generalize the method for finite nuclear and density contrast, using fillable objects such as spheres, as will be shown later.

This resolution measurement is verified from CT data of the HCR phantom reconstructed using various Siemens CT kernels with known MTFs. The results have an error margin within ±10% (or ±0.1 mm) compared to the documented resolution values.[24]

Setting 2: HCS

In this setting, the HCS phantom is used to measure both noise and resolution. As in setting 1, the noise metric is defined as the ratio of SD over the mean in a large uniform VOI, as shown in Figure 3, where the light pink region is the VOI used for noise measurement. Note that the voids in the VOI are the supporting rods, which cannot contribute to the uniform background.

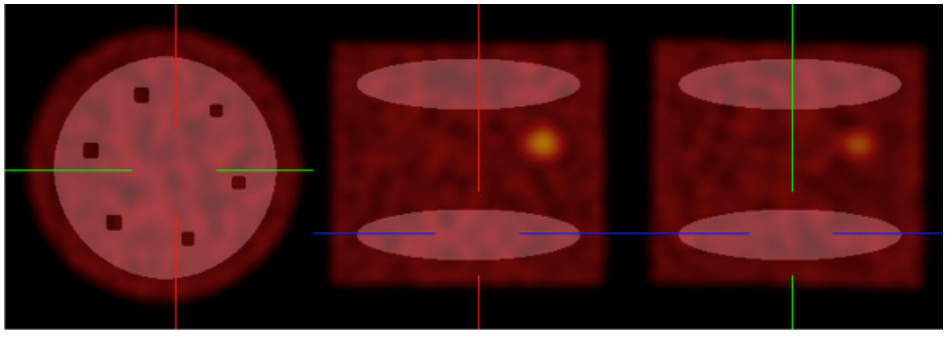

Figure 3: VOI inside uniform cylinder phantom for noise measurement. The light pink regions inside the phantom are the selected spherical VOIs.

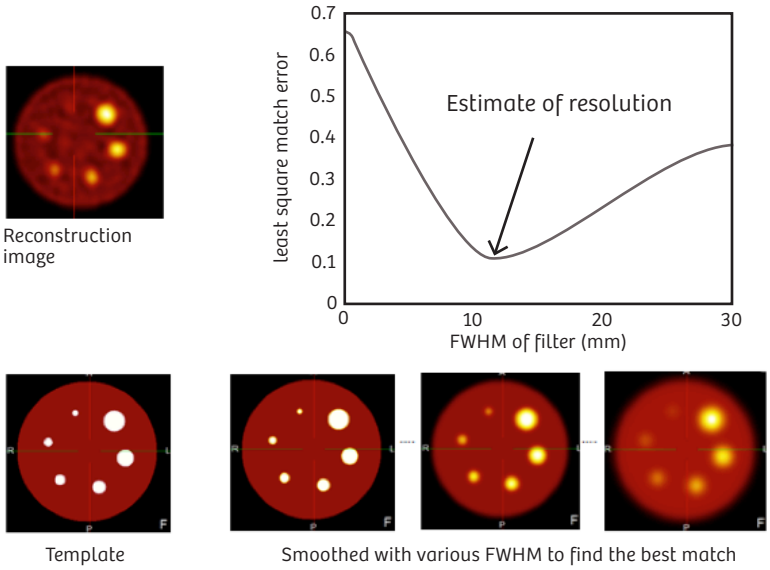

Figure 4: Illustration of resolution measurement using matched filter for HCS. Given a real reconstructed image, the template is smoothed with Gaussian filters of various FWHM, and the difference square between the real image and filtered template is calculated. The FWHM, which gives the smallest difference, is recognized as the resolution.

The resolution estimated with the matched filter method is similar to that of HCR as shown in Figure 4. The template of the HCS phantom is a geometric model based on the positions and diameters of the spheres, and adapted appropriately for the inner diameters. The image intensity values of the template are assigned based on the activity concentration in the background and spheres. The template is filtered with 3-D Gaussian kernels of various FWHM ("probing" filter), and resolution is defined as the FWHM minimizing the matched error.

Data acquisition and reconstruction

The uniform HCR and HCS data are acquired with a clinically representative Symbia™ T series test system in the lab, which was calibrated and quality-controlled for clinical use as recommended by the factory. The acquisition settings are shown in Table 1. Projections are acquired with 120 views (3-degree angular step), and are sub-sampled to 60 views (6-degree angular step), step-and-shoot.

We used four reconstruction methods: (1) xSPECT Quant (xQ), (2) xSPECT Bone™ (xB), (3) Flash 3D (F3D) and (4) OSEM, but using the xSPECT formalism (xEMAS; xE) at 12, 24, 48, 96, 192, 480 and 960 updates, with one subset, 10 mm post-smoothing and CT-based attenuation correction and scatter correction. The same registration matrix was used for all data. xE is based upon OSEM, but uses the projection operator employed in xSPECT, and is currently not commercially available. The comparison to xE gives insight into the effect of projection operator accuracy versus the update method itself.

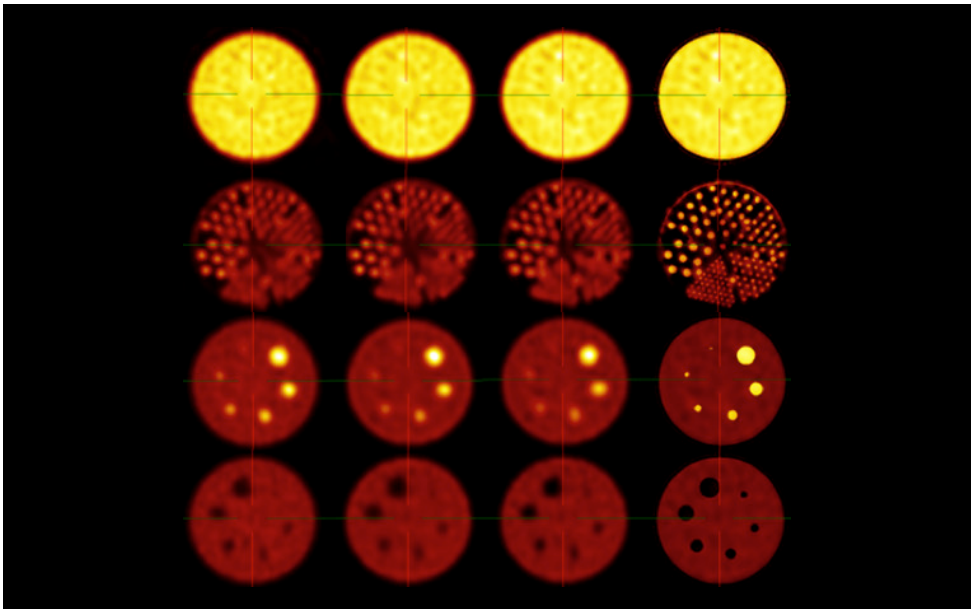

Figure 5: Phantom reconstructions with four methods with 3-degree angular sampling, 96 updates (F3D and xE) or 24 updates (xQ and xB). From left to right: F3D, xE, xQ and xB. From top to bottom: uniform cylinder, HCR, hot spheres in HCS, cold spheres in HCS.

Results and analysis

Figure 5 shows examples of reconstructions of uniform, HCR and HCS phantoms using four methods (from left to right): F3D, xE, xQ and xB. Visually, xB reconstructions have clearly higher resolution than the other three. xQ has slightly better resolution than F3D, especially for cold spheres.

Acquisition Setting	Uniform	HCR	HCS
Injected dose ^{99M}Tc (MBq)	580	370	370
Total counts (M10^6)	22.1	17.6	23.1
Count density (256 Matrix)	5.37/pixel; 0.93/mm^2	4.26/pixel; 0.74/mm^2	9.71/pixel; 1.69/mm^2
Number of projections for 360°	120	120	120
Symbia T16 CT model and slice thickness (mm)	3	3	3

Table 1: Summary of phantom acquisition.

Figure 6 shows the noise and resolution after various iteration updates for the four methods. For the same method, results from 3-degree sampled data have at least 20% lower noise than those for 6-degree sampling. At the same number of updates, xQ has clearly better resolution than F3D, and xB has significantly better resolution than either of the others. The update number, however, is method-specific and not recommended for comparing different methods.

Instead, resolution recovery versus noise is plotted, yielding a resolution per unit noise measure that allows for direct comparison of different reconstructions. The resolution versus noise relations are shown in Figure 6 and the lower panel of Figure 7, below. At the clinical noise scheme 0.05-0.1, xQ has slightly smaller FWHM than F3D, and xB significantly higher resolution than either. Comparing the two different angular sampling method scenarios of the same reconstruction methods, 3-degree data have about 10% higher resolution than did 6-degree data at the same noise level. Our investigation using an image review by five experienced physicians shows no clinically significant difference between xQ and xE, provided that reading training was provided, thus allowing habituation of readers to certain idiosyncrasies of the image; both methods were an improvement over F3D. This indicates that the improvements result from a more accurate system matrix modelling, rather than the update scheme, as xQ and xE use the same projection operator but different update schemes.

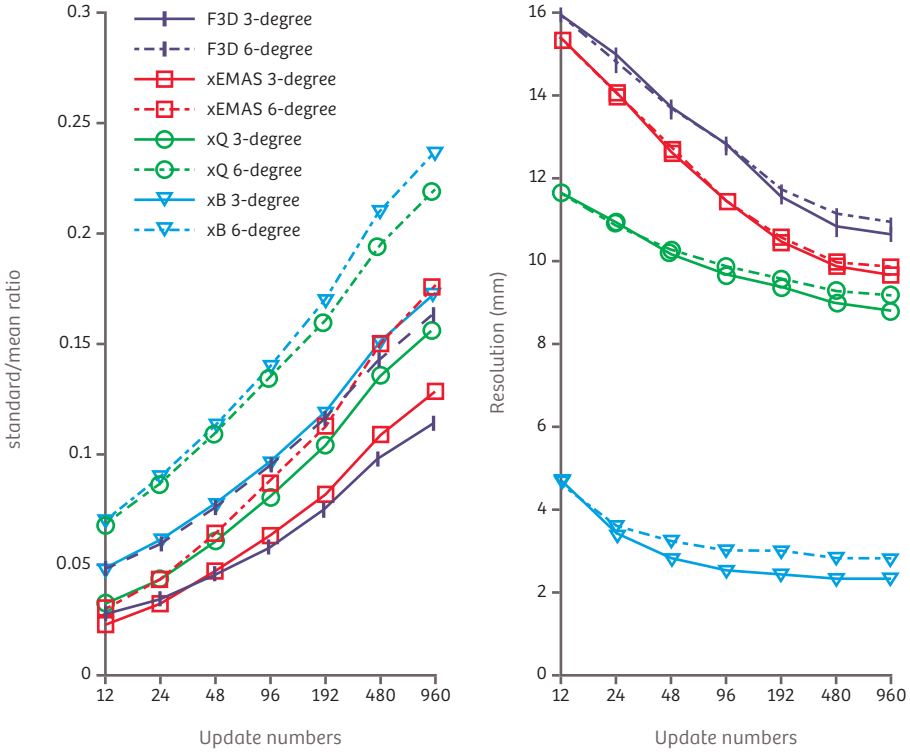

Figure 6: Noise and resolution setting 1 (cylinder+HCR) of four methods with 3-degree and 6-degree angular sampling, all with 1 subset and 10 mm post-smoothing. The left upper panel shows the noise level at various updates, computed from the uniform phantom. The upper right panel shows the resolution recovery at various updates, estimated from HCR phantom using matched filter method.

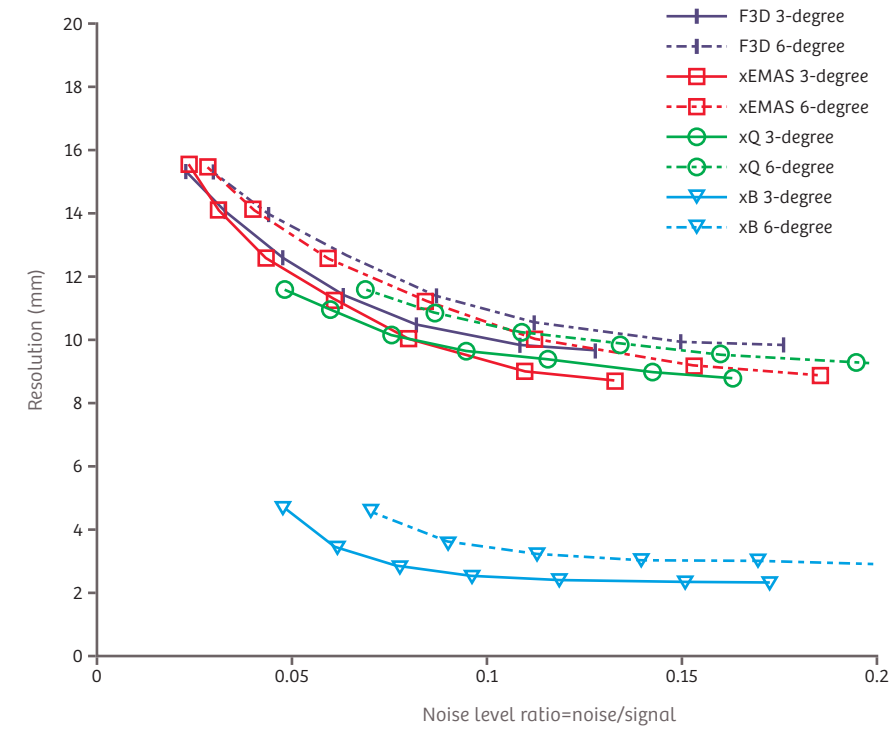

Figure 7: Resolution of hot rods versus noise in setting 120 (Cylinder+HCR) for four methods with 3-degree and 6-degree angular sampling, all with 1 subset and 10 mm post-smoothing. The noise is calculated from uniform phantom, and resolution is estimated from HCR phantom using the matched filter method.

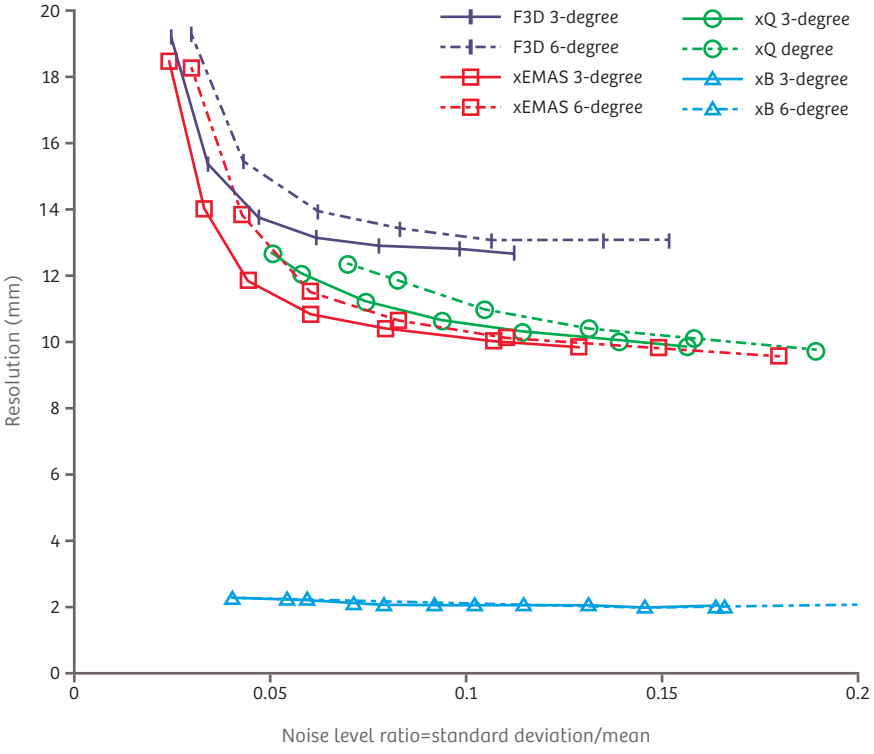

Figure 8: Resolution of hot spheres versus noise in setting 2 (HCS) for four methods with 3-degree and 6-degree angular sampling, all with 1 subset and 10 mm post-smoothing. The noise is calculated from uniform background of HCS, and resolution is estimated from hot spheres in HCS phantom using matched filter method.

Similarly, the resolution versus noise in setting 2 is plotted for hot spheres and cold spheres in Figure 8 and Figure 9, respectively. Although the values of resolution are not exactly the same as in setting 1, similar trends are observed:

1. xQ has better resolution than F3D, especially for cold spheres where xQ has ≈20% smaller FWHM;
2. xE and xQ have similar performance;
3. xB has considerably higher resolution than the other three;
4. 3-degree sampling has ≈10% higher resolution than 6-degree sampling in the same method (except xB, for which resolution is largely determined by extra modal information from CT).

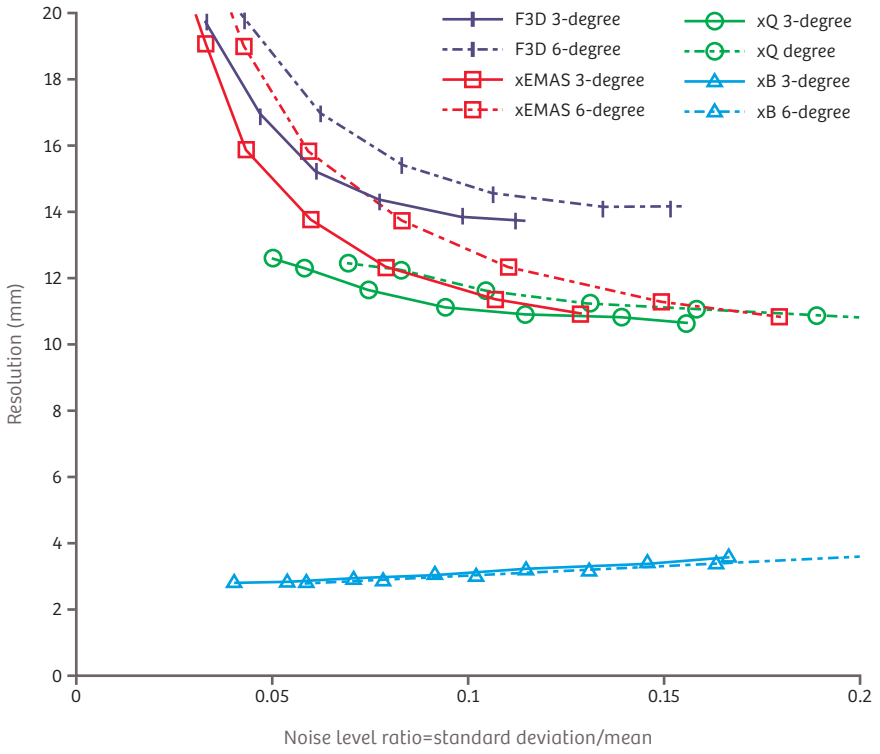

Figure 9: Resolution of cold spheres versus noise in setting 2 (HCS) for 4 methods with 3-degree and 6-degree angular sampling, all with 1 subset and 10 mm post-smoothing. The noise is calculated from uniform background of HCS, and resolution is estimated from cold spheres in HCS phantom using matched filter method.

In Table 2, the resolution of HCR, hot spheres and cold spheres at noise level 0.075 is listed, which is the middle point of the practical clinical range 0.05-0.1, which further confirms the above observations. The standard deviation is estimated by bootstrapping.

Reconstruction Methods	Hot Rods in HCR	Hot Spheres in HCS	Cold Spheres in HCS
F3D 3-degree	10.8±0.3	12.9±0.4	14.4±0.5
F3D 6-degree	12.1±0.4	13.6±0.4	16.0±0.6
xE 3-degree	10.4±0.3	10.5±0.3	12.6±0.4
xE 6-degree	11.8±0.3	10.9±0.4	14.4±0.5
xQ 3-degree	10.2±0.3	11.2±0.3	11.5±0.4
xQ 6-degree	11.3±0.3	12.2±0.3	12.3±0.4
xB 3-degree	2.9±0.3	2.1±0.2	2.9±0.3
xB 6-degree	4.4±0.4	2.1±0.3	2.8±0.3

Table 2. Resolution (in mm) at noise level 0.075.

Quantitation evaluation of xSPECT

Methods and materials

Unlike traditional SPECT that reconstructs images in the unit of count-per-voxel, xSPECT provides a quantitative solution by measuring the activity concentration in Bq/ml at a given reference time (injection time is chosen).

In this section, the evaluation of quantitative accuracy of xSPECT is discussed.

For xQ and xB, a NIST-traceable calibration using a source (Calibrated Sensitivity Source (CSS)) is employed. The hot-cold-sphere phantom is loaded with ^{99m}Tc activity concentration of 73.5 kBq/ml in the background, and 381.8 kBq/ml in the hot spheres. The contrast ratio between spheres and background is thus about 5.2. The error of determining the injected activity concentration is estimated at about 1%. The goal of the CSS calibration is to standardize the system sensitivity, which is essential for quantitative results that can be compared across systems and time. Each CSS contains an activity accurate to within a 3%-(99% CL or 2.56 ∑) traceable uncertainty of the known manufactured strength, which itself resides within a 15% acceptance range of the nominal 111 MBq. Following proper calibration, where the CSS is attached to the integrated source holder and extended into the FOV at a precise location, the xSPECT system is designed to estimate the activity concentration as an integral part of the reconstruction process. The result is an image in units of Bq/ml, requiring no further conversion. Indeed, all corrections occur in image space, allowing the data to remain unadulterated Poisson variables throughout the reconstruction process.

The same hot-cold-sphere (HCS) phantom data as in the noise/resolution test is used to perform the quantitation test. Refer to appendix 1 for the detailed instruction of the phantom loading. Before acquisition of the data, the injected concentration and injection time is recorded. The acquisition settings are shown in Table 1. Projections are acquired with 120 views (3-degree angular step), and are sub-sampled to 60 views (6-degree angular step). Since F3D is not quantitative, only xQ, xB and xE reconstructed images were evaluated. Note that xB is the same method as xQ but with additional use of CT information. All images are reconstructed in kBq/ml, corrected to injection time.

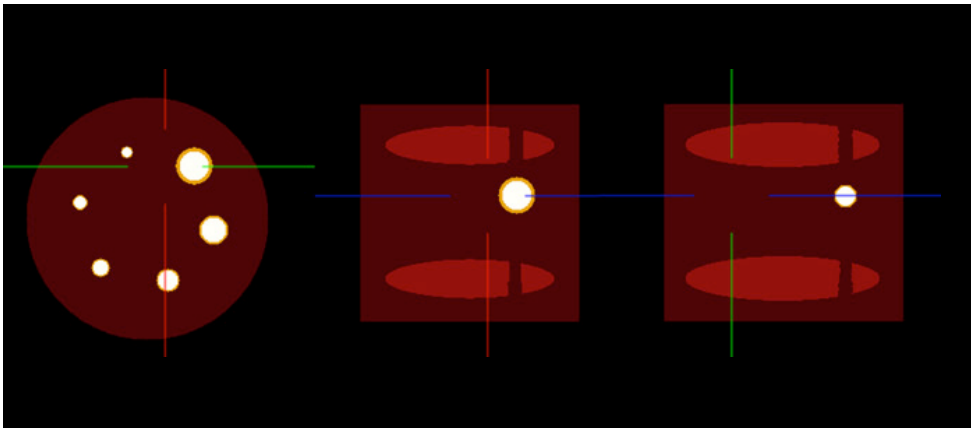

Figure 10: VOI inside uniform cylinder phantom for measuring background and 6 spheres.

Mean activity concentration (in kBq/ml) is measured for background and 6 hot spheres (Figure 10). For background, a large uniform VOI is chosen, shown as the two red elliptical regions in the upper and lower part of the phantom. As above, the voids in the VOI are the supporting rods. xB is treated differently than xQ and xE when measuring activity in spheres. Considering the partial volume effect of xQ and xE, a sphere VOI with 80% of the physical diameter of each sphere is chosen, which resembles the method described in reference 25. The reduced sphere VOIs are shown in white in Figure 10. In xB, partial volume effect is considerably reduced by using the zoning method. Hence, the full volume of the spheres is used to measure the mean activity. The full diameter is indicated by the yellow ring in Figure 10. Table 3 shows the dimensions of the physical spheres and reduced VOIs. Note that in real measures, the diameters and volumes are approximations of these numbers due to the limit imposed by voxel size of the reconstructed image.

Sphere index	Physical diameter in mm	Physical volume in ml	Diameter of reduced VOI in mm	Volume of reduced VOI in ml
1	9.8	0.5	7.9	0.3
2	12.4	1.0	9.9	0.5
3	15.6	2.0	12.5	1.0
4	19.7	4.0	15.8	2.1
5	24.8	8.0	19.9	4.1
6	31.2	16.0	25.0	8.2

Table 3: Diameter (in mm) and volume (in ml) of 6 spheres and VOIs.

Results and analysis

Figure 11 shows the quantitation results of the background and 6 spheres using xE, xQ and xB with 3-degree and 6-degree angular sampling after various updates. The upper left shows the results of the background, and lower 6 panels show results from sphere 1 to sphere 6. In all the figures, the curves show the mean activity concentration versus update number. The ground truth (background 73.5 kBq/ml, sphere 381.8 kBq/ml) is also drawn as reference.

From the figures, which are based on measurements in a single system, we draw a number of general conclusions:

1. All methods give very accurate estimates (close to 100%) of the background, and the results are stable with updates. This is reasonable because a large background VOI is chosen for the estimation, which is robust to noise. The partial volume effect is also largely eliminated.
2. For spheres, quantitation accuracy is improved with increased number of updates, but all are underestimated due to partial volume effects (except xB on the largest sphere). However, a very high update number is not recommended because that would iterate to higher noise. For xQ and xB, update range 24-96 is recommended, and for xE 48-196 is recommended.
3. Quantitation accuracy is improved with increased size of spheres. This can be explained by the relative reach of partial volume effect compared to the sphere size.
4. In early updates (<48), xQ recovers contrast and resolution more rapidly than xE due to xQ's faster conjugate gradient scheme. After 48 updates, xE and xQ have similar performance. xB has significantly better results than both. On the largest sphere, xB yields results very close to truth.
5. The 3-degree and 6-degree angular sampling have similar performance for all three methods.

To more clearly show the relation between quantitation and sphere size, we chose fixed update number of 48. The results are summarized in Figure 12, which shows the mean activity concentration in background and 6 spheres, whereas Table 4 shows the relative accuracy compared to truth. For background, all methods give estimation within 1% of the truth. For spheres, xE and xQ have almost overlapping curves. Their accuracy gradually improves with increasing size of spheres, and reaches over 90% accuracy for the largest sphere (16 ml). xB gives much higher recovery (>60%) even for the smallest sphere (0.5 ml), which rises to close to 100% for the largest sphere (16 ml). This suggests that xB not only produces considerably higher resolution, but also yields more accurate quantitation estimation, given that the zoning is correct.

It is worthwhile to point out that OSEM reconstruction with 3D collimation modelling produces, for cases with sharp edges and high contrast, a Gibbs edge enhancement. Furthermore, such edge overshoot can be amplified in small structures, with edges lying in close proximity to each other (<FWHM of PSF), such that the Gibbs edge overshoot appears to create a hotter center than expected. Such overshoot is highly dependent on the update number, and could somewhat compensate for partial volume-induced depression. The tendency of Gibbs edge ringing is reduced with an additive update mechanism such as OSCG compared to OSEM. We represent the reconstruction in 256 by matrix with 2.4 mm pixel size, which implies that when the VOI is defined with 80% of the sphere diameter, it is represented by at least 3-4 voxels in a line, as Table 3 shows.

Figure 11: The quantitation results of background and 6 spheres using the xE, xQ and xB at various updates.

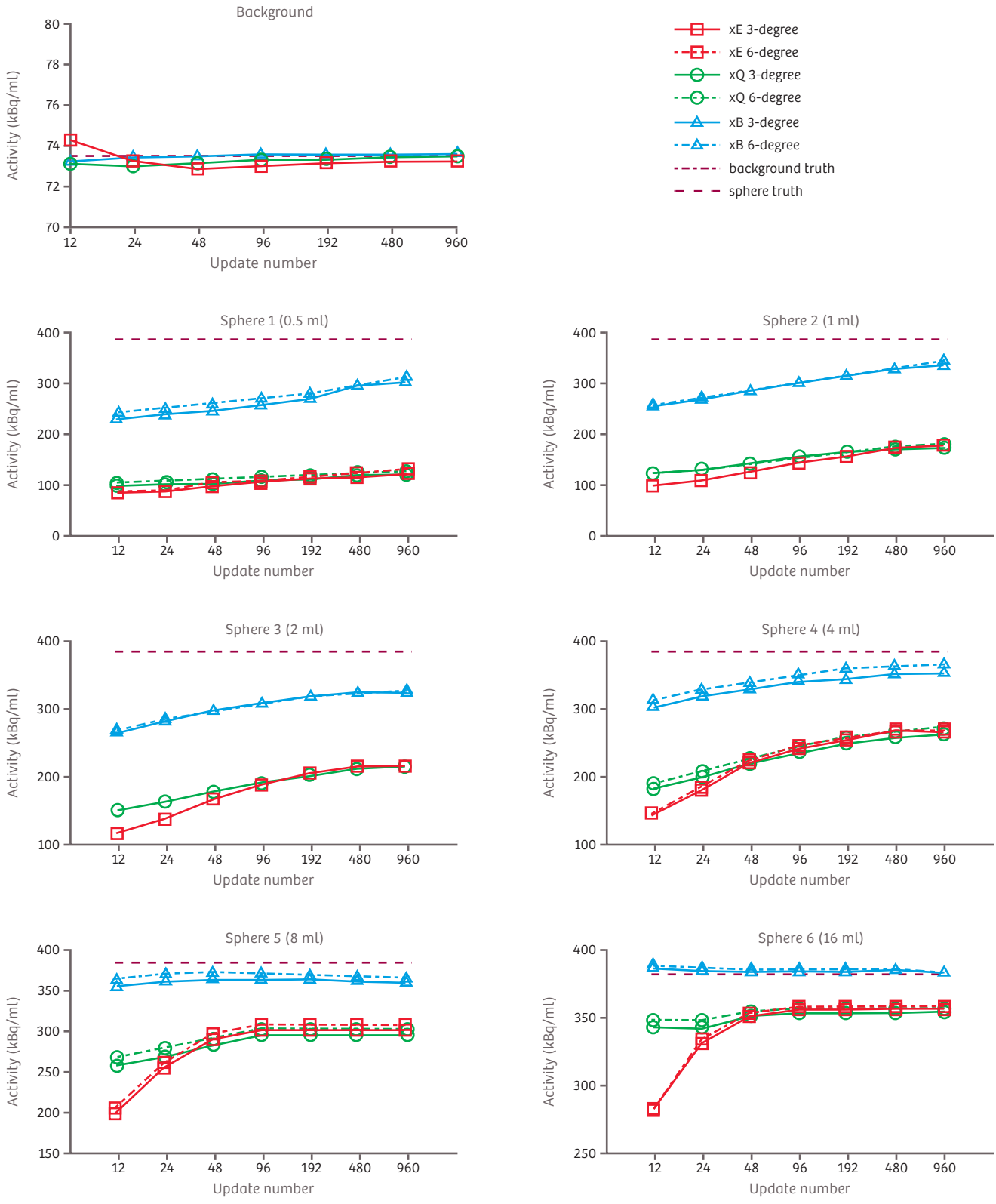

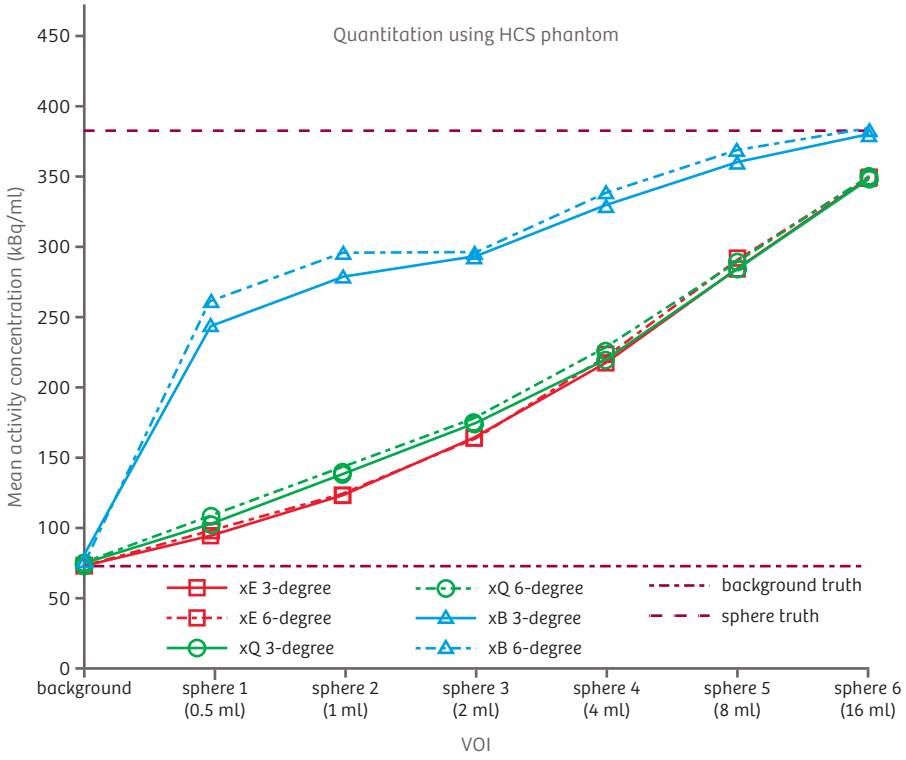

Figure 12: Quantitation results of xE, xQ and xB for background and spheres. All after 48 updates.

Consequently, we do not sample only the center voxel, which is highly susceptible to Gibbs enhancement, especially for the smaller spheres. By using a different update method to reduce Gibbs effects, increasing the spatial sampling, and selecting a procedure to measure activity concentration in a VOI at 80% diameter in xQ, but at 100% diameter in xB (where the real boundary is known from the CT), we endeavor to increase reproducibility over a large range of updates. This holds even for smaller spheres that otherwise would suffer from update-dependent recovery coefficients. Still, we do not obtain an explicit partial volume correction, which is an improvement to be implemented in the future.

Method	Background	Sphere 1	Sphere 2	Sphere 3	Sphere 4	Sphere 5	Sphere 6
xE 3-degree	99.1%	24.8%	32.3%	43.1%	57.2%	75.0%	91.9%
xE 6-degree	99.0%	25.9%	32.5%	43.2%	59.0%	77.2%	92.5%
xQ 3-degree	99.5%	27.0%	36.3%	45.8%	57.8%	74.6%	91.9%
xQ 6-degree	99.4%	28.6%	36.9%	46.2%	59.6%	76.5%	92.5%
xB 3-degree	100.0%	64.4%	73.7%	77.2%	86.8%	95.0%	100.1%
xB 6-degree	100.0%	68.8%	78.0%	78.0%	89.4%	97.1%	101.0%

Table 4: Relative quantitation accuracy of background and 6 spheres after 48 updates.

Summary

The introduction of xSPECT represents a paradigm shift, constituting our concerted attempt to carefully optimize calibration, acquisition and reconstruction to meet the stringent needs of absolute quantitation in SPECT. To this end, we make use of an independent absolute standard (3%-traceable NIST source) for both the dose calibrator and the imaging system itself. xSPECT incorporates an additive update mechanism, a more accurate model of the image formation physics using a measured collimator PSF over the entire FOV of the detector at various heights, and the use of extra-modal information to enhance nuclear imaging reconstructions. This paper investigates the xSPECT reconstruction from the joint perspective of image quality and quantitation.

We develop a general approach to report some basic measures of image quality, notably resolution as a function of unit noise, where resolution is derived from the edge response of an extended object. Based on experience to date, such resolution characterization translates more readily to clinical reality, as it removes idiosyncrasies in reconstruction stemming from very small objects with infinitely high contrast (e.g., point/line source in air). At a given noise level, xQ shows better resolution than the current standard, i.e., the F3D method. Especially for cold regions, xQ has >20% higher resolution than F3D. xE has the same physics model as xQ, but uses the OSEM update scheme. Based on the similar performances of xQ and xE, the advantages of xSPECT over F3D can be attributed mainly, but not exclusively, to the improved accuracy of the image formation model used in xSPECT. We also show that 6-degree angular sampling yields slightly higher noise and lower resolution compared to 3-degree sampling.

xB imaging of bone benefits from the significantly higher resolution at the CT delineated edges than is afforded by F3D and xQ, which is consistent with the known CT resolution. Ultimately, the clinical resolution of xSPECT depends on whether or not one considers the resolution at the CT delineated edge to fall between emission zones, or within the interior of an emission zone.

Quantitation accuracy of xE, xQ and xB was assessed on a single system, in one filling scenario, and using a precision source. Given these conditions, all the methods give estimates on the background, within 1% of error compared to truth. For spheres, xE and xQ have similar performance. We see underestimating in small spheres, but quantitation accuracy gradually rises for spheres of increasing size, achieving over 90% accuracy for the largest sphere (16 ml). xB gives much higher recovery (>60%) even for the smallest sphere (0.5 ml), and reaches 1% error margin for the largest sphere (16 ml). We also found that the quantitation improves with higher iterations, but the choice of iteration number is a trade-off between image quality and quantitation. A significant difference on quantitation between 3-degree and 6-degree sampling was not found.

As an addendum to these investigations, we offer some hints and tips for xSPECT reconstruction. In general terms, we suggest the following guidelines: acquire a CT with good image quality; properly register the SPECT to the CT; obtain a complete record of injected dose, time and patient information; and, finally, perform proper system calibration. The selection of optimal parameters should be guided by the individual case's count level.

Appendix 1: Instructions for quantitative loading of a hot-cold spheres phantom for testing xSPECT Bone/xSPECT Quant

The procedure detailed below is meant to be used with a Data Spectrum Cylinder Phantom with Data Spectrum acrylic hollow sphere sets. The procedure is also specific to using the CT contrast agent specified below and not for contrast agents with a different iodine concentration. The contrast zoning parameters used during reconstruction for this test are not user-definable and, as such, the test will not work if using glass spheres instead of acrylic spheres, or if using a CT contrast agent with iodine concentration that is different from what is specified below.

The objective is to prepare a phantom having 3 zones, i.e., Hot Spheres, Cold Spheres (including the cylindrical container) and Background. The pre-defined zoning for this phantom requires that:

1. The Hounsfield Value in the Hot Spheres is centered around 350.
2. The Hounsfield Value in the Cold Spheres is centered around 150 (which is the same as that for the acrylic used to make the phantom).

The following dilutions to achieve the objectives above should be made:

1. For the background, prepare a large dilution (8 liters) of water and pertechnate to achieve the desired background concentration, e.g., 16 mCi (592 MBq) for an activity concentration of 2 µCi/ml (74 kBq/ml).
2. For Hot Spheres, make a 6% by volume dilution of Conray CT Contrast (Iothalamate Meglumine Injection USP 60%—600 mg/ml Iothalamate Meglumine, and 282 mg/ml organically-bound Iodine) and water, e.g., 188 cc water+12 cc contrast for a 200 cc dilution. To this dilution, add pertechnate based on the desired nuclear contrast, e.g., 2 mCi (74 MBq) for a 5X or 4 mCi (148 MBq) for a 10X nuclear contrast.
3. For the Cold Spheres, make a 2.5% by volume dilution of Conray CT Contrast (Iothalamate Meglumine Injection USP 60%—600 mg/ml Iothalamate Meglumine, and 282 mg/ml organically-bound Iodine) and water, e.g., 195 cc water+5 cc contrast for a 200 cc dilution.

Fill the two sets of hollow spheres with the two dilutions prepared above, ensuring that there are no bubbles inside the spheres. Attach the spheres to the cylinder and fill the cylinder with the background dilution ensuring that there are a minimal number of bubbles in the background volume.

The phantom prepared above should be scanned using the clinical SPECT/CT protocol for bone scans, and the resulting projection data can be reconstructed using F3D, xQ or xB reconstruction engine using the “Contrast Zone” class. The difference in reconstructed image quality between data reconstructed with and without zoning can be evaluated in a fusion display, and quantitative accuracy of activity concentration (Bq/ml) can be evaluated using volumetric analysis.

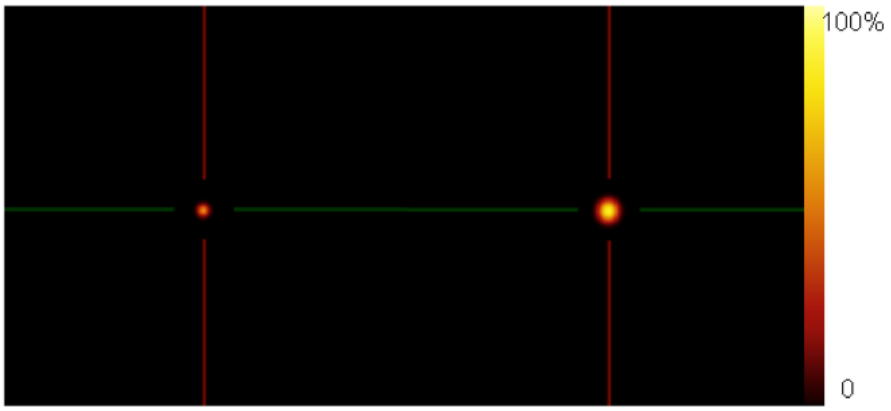

Figure 13: Reconstructions of a point source from F3D (left) and xQ (right). Both have 96 updates and 5 mm post-smoothing.

Appendix 2: Recovery of a singular point source

An OSEM-based reconstruction (multiplicative update) such as F3D or xE can converge faster than a minimizer-based reconstruction (additive update) for one singular point source in air and its convergence depends on the minimizer and its pre-conditioner, the objective function, and its weighting scheme. We briefly discuss the issue using F3D and xQ as examples. As shown in Figure 13, the F3D result converges to a point as small as a single voxel, but the xQ has a slow converging rate and produces a hot "ball" with a size considerably larger than the F3D result.

What is the reason for xQ's slow recovery? Some insight can be obtained from analysis with the Mighell Chi square merit function:

$$\chi^2 = \sum_i \frac{\left(d_i + 1_{d_i>0} - m_i\right)^2}{d_i + 1}$$

where i is the pixel index, d_i is the projection data at pixel i, and m_i is the data model at pixel i. This merit function can be rewritten in matrix notation. Let D denote the vectorized projection data, I denote the lexicographically ordered image vector and H denote the forward projection matrix. Using this notation, the data model M can be defined as M=HI. The merit function and its gradient with respect to the image may then be expressed as follows in equations (3) and (4), respectively:

3. $$\chi^2 = (D - M)^T (D + 1)^{-1} (D - M)$$

4. $$\nabla_I = H^T (D + 1)^{-1} (D - M)$$

In the gradient, the difference between the data and data model is weighted by the inverse of the projection data. This implies that hot pixels have lower weights and cold pixels have higher weights. For a very hot point source or a small object, very low weight is applied to the hot projection region, which leads to the slow recovery in the iterative reconstruction. In other words, the reconstruction focuses on the entire image rather than the single focal point of interest.

The merit function can be modified in such a way that the weights are uniformly distributed in the projection space (known as the unweighted least squares method) as shown in equations (5) and (6):

5. $$\chi^2 = \sum_i (d_i - m_i)^2 = (D - M)^T (D - M)$$

6. $$\nabla_I = H^T (D - M)$$

In this case, much faster recovery is achieved for the point source, as seen in Figure 14. However, the drawback of the unweighted least squares method is that the implications of noise are not taken into account, resulting in a noisier warm background in the hot and cold spheres (HCS) phantom image.

One could also use a merit function which represents a compromise between the previous two and involves a weighting by the inverse of the square root of the data, as represented in (7) and (8):

7. $$\chi^2 = \sum_i \frac{(d_i - m_i)^2}{\sqrt{d_i + 1}} = (D - M)^T \sqrt{(D + 1)^{-1}} (D - M)$$

8. $$\nabla_I = H^T \sqrt{(D + 1)^{-1}} (D - M)$$

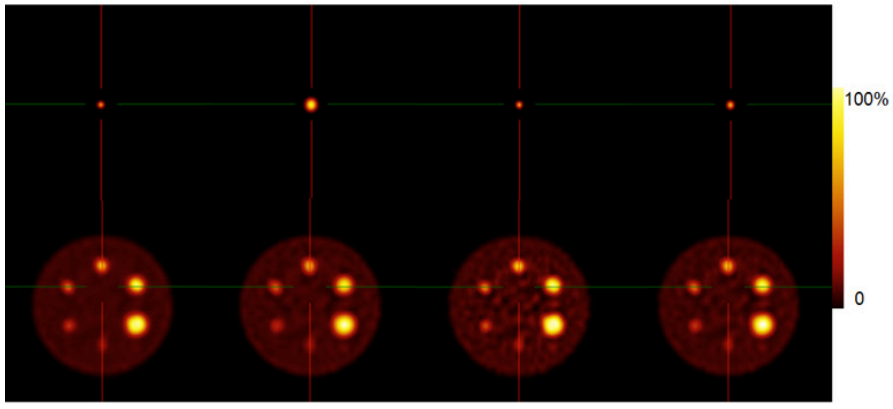

Figure 14: Reconstruction of a point source (top) and HCS phantom (bottom) from the four methods. From left to right, F3D, xQ with Mighell Chi square, xQ with unweighted least squares, xQ with least squares and square root weight.

As expected, the result of this choice falls somewhere between the previous two results. The point recovery is faster than Mighell's Chi square, but slightly slower than that of unweighted least squares. Similarly, the noise level in the HCS warm background is higher than Mighell's, but lower than in the unweighted case. The estimated FHWM of reconstructed point source after 96 updates is listed in Table 5, which confirms the above observations.

Across the vast majority of applications, the hot, solitary point source scenario is a clinically irrelevant case. In usual phantom studies and clinical practice, the gaps between hot and cold regions are generally not very large. In these scenarios, the advantages for quantitative imaging of extended sources offered by Mighell's Chi square is more valuable than the ability to reconstruct an isolated point source.

Method	FHWM of Point Source (mm)
F3D	4.3
xQ with Mighell's Chi square (standard)	9.4
xQ with unweighted least squares	5.1
xQ with square root weight	6.3

Table 5: FHWM of reconstructed point source at 96 updates.

Authors

A. Hans Vija, PhD
Dr. Alexander Hans Vija is the head of the SPECT research team at Siemens Healthineers, Molecular Imaging. He earned his Ph.D. in Physics in 2001 from the University of Washington, Seattle.

Dr. Vija and his team developed technology behind the products: Flash 3D, Attenuation Correction, Enhanced Planar Processing, IQ•SPECT, xSPECT Quant and xSPECT Bone, and Symbia and Symbia Intevo SPECT/CT systems. He also established, and is conducting worldwide, clinical research collaborations.

He has over 20 publications and holds over 40 US patents and was awarded the "Inventor of the Year" of Siemens AG in 2013.

References

[1] A. H. Vija, "Introduction to xSPECT Technology: Evolving Multi-modal SPECT to Become Context Based and Quantitative.," Siemens Medical Solutions USA, Inc., Molecular Imaging, White Paper, 2013.

[2] D. W. Wilson and B. M. W. Tsui, "Noise Properties of Filtered-Backprojection and ML-EM Reconstructed Emission Tomographic Images," IEEE Transactions on Nuclear Science, vol. 40, pp. 1198-1203, 1993.

[3] H. H. Barrett, "Noise properties of the EM algorithm: I. Theory," Phys. Med. Biol., vol. 39, pp. 833-846, 1994

[4] D. W. Wilson, B. M. W. Tsui, and H. H. Barrett, "Noise properties of the EM algorithm. II. Monte Carlo simulations," Physics in Medicine and Biology, vol. 39, pp. 847-871, 1994.

[5] S. J. Glick and E. J. Soares, "Noise Characteristics of SPECT Iterative Reconstruction with a Mis-Matched Projector-Backprojector Pair," IEEE Transactions on Nuclear Science, vol. 45, 1998.

[6] D. S. Lalush and B. M. W. Tsui, "Mean-Variance Analysis of Block-Iterative Reconstruction Algorithms Modeling 3D Detector Response in SPECT," IEEE Transactions on Nuclear Science, vol. 45, pp. 1280-1287, 1998.

[7] D. J. Kadrmas, E. V. R. DiBella, R. H. Huesman, and G. T. Gullberg, "Analytical propagation of errors in dynamic SPECT: Estimators, degrading factors, bias and noise," Physics in Medicine and Biology, vol. 44, pp. 1997-2014, 1999.

[8] J. Nuyts, "On Estimating the Variance of Smoothed MLEM Images," IEEE Transactions on Nuclear Science, vol. 49, pp. 714-721, 2002.

[9] P. Razifar, M. Sandstroem, H. Schnieder, B. Langstroem, E. Maripuu, E. Bengtsson, et al., "Noise correlation in PET, CT, SPECT and PET/CT data evaluated using autocorrelation function: a phantom study on data, reconstructed using FBP and OSEM," BMC Medical Imaging, vol. 5, 2005.

[10] B. M. W. Tsui, Z. Xide, E. C. Frey, and G. T. Gullberg, "Properties Of Iterative Algorithms In SPECT Image Reconstruction," in Nuclear Science Symposium, 1990. Conference record: Including Sessions on Nuclear Power Systems and Medical Imaging Conference, 1990 IEEE, 1990, pp. 1467-1474.

[11] B. M. W. Tsui, X. Zhao, E. C. Frey, and G. T. Gullbert, "Comparison Between ML-EM and WLS-CG Algorithms for SPECT IMage Reconstruction," IEEE Transactions on Nuclear Science, vol. 38, pp. 1766-1772, 1991.

[12] I. A. E. Agency, "IAEA Health Series No. 6," in Quality Assurance for SPECT Systems, ed. Vienna, Austria: IAEA, 2009.

[13] N. E. M. Association, "NEMA Standards Publication No. NU 1," in Performance Measurements of Scintillation Cameras, ed. Washington, D.C.: NEMA, 2007.

[14] J. A. Fessler and W. L. Rogers, "Spatial Resolution Properties of Penalized-Likelihood Image Reconstruction: Space-Invariant Tomographs," IEEE Transactions on Image Processing, vol. 5, pp. 1346-1358, 1996.

[15] J. W. Stayman and J. A. Fessler, "Compensation for Nonuniform Resolution Using Penalized-Likelihood Reconstruction in Space-Variant Imaging Systems," IEEE Transactions on Medical Imaging, vol. 23, 2004.

[16] D. Badger and L. Barnden, "Spatial resolution is dependent on image content for SPECT with iterative reconstruction incorporating distance dependent resolution (DDR) correction," Australasian Physical & Engineering Sciences in Medicine, pp. 1-7, 2014.

[17] I. A. Cunningham and A. Fenster, "A method for modulation transfer function determination from edge profiles with correction for finite-element differentiation," Medical Physics, vol. 17, pp. 533-537, 1986.

[18] A. H. Vija, E. G. Hawman, and J. C. Engdahl, "Analysis of a SPECT OSEM Reconstruction Method with 3D Beam Modeling and Optional Attenuation Correction: Phantom Studies," in IEEE Nuclear Science Symposium and Medical Imaging Conference, 2003, pp. 2662-2666.

[19] J. A. Siegel, S. R. Thomas, J. B. Stubbs, M. G. Stabin, M. T. Hays, K. F. Koral, et al., "MIRD Pamphlet No. 16: Techniques for Quantitative Radiopharmaceutical Biodistribution Data Acquisition and Analysis for Use in Human Radiation Dose Estimates," Journal of Nuclear Medicine, vol. 40, pp. 37S-61S, 1999.

[20] M. Stabin and A. B. Brill, "Physics Applications in Nuclear Medicine: 2007," Journal of Nuclear Medicine, vol. 49, pp. 20N-25, February 1, 2008 2008.

[21] J. Ma and A. H. Vija, "Noise and resolution character- istics for xSPECT reconstruction method," J Nucl Med Meeting Abstracts vol. 55, pp. 2129-, May 1, 2014 2014.

[22] J. Ma and A. H. Vija, "Comparison of Multi Modal SPECT Reconstruction Methods Using a Clinically Relevant Assessment of the Image Resolution at Various Noise Levels," IEEE Medical Imaging Conference Record, 2014.

[23] Data Spectrum. (http://www.spect.com/products-spect. html)

[24] "Somatom Emotion System Owner Manual," Siemens Healthcare, System Manual 2012.

[25] A. Seret, D. Nguyen, and C. Bernard, "Quantitative capabilities of four state-of-the-art SPECT-CT cameras," European Journal of Nuclear Medicine and Molecular Imaging, vol. 2, 2012.

The products/features and/or service offerings (here mentioned) are not commercially available in all countries and/or for all modalities. If the services are not marketed in countries due to regulatory or other reasons, the service offering cannot be guaranteed. Please contact your local Siemens organization for further details.

xSPECT Quant, Symbia Intevo Bold and Broad Quantification are not commercially available in some countries. Due to regulatory reasons, their future availability cannot be guaranteed. Please contact your local Siemens organization for further details.

^{177}Lu is not currently recognized by the US FDA as being safe and effective, and Siemens does not make any claims regarding its use. Due to regulatory reasons, its future availability cannot be guaranteed. Please contact your local Siemens organization for further details.

Siemens Healthcare Headquarters
Siemens Healthcare GmbH
Henkestr. 127
91052 Erlangen
Germany
Phone: +49 9131 84-0
siemens.com/healthcare

Global Business Line
Siemens Medical Solutions USA, Inc.
Molecular Imaging
2501 North Barrington Road
Hoffman Estates, IL 60192
USA
Phone: +1 847 304-7700
siemens.com/mi

Order No. A91MI-10462-T1-7600 | Printed in USA | MI-2735.TM.JV.TW.1500 | © Siemens Healthcare GmbH, 09.2017